INSTITUTE OF PHYSICS PUBLISHING MODELLING AND SIMULATION IN MATERIALS SCIENCE AND ENGINEERING

Modelling Simul. Mater. Sci. Eng. **11** (2003) 457–475 PII: S0965-0393(03)62956-6

Micromechanics simulations of glass–estane mock polymer bonded explosives

Biswajit Banerjee[1,3], **Carl M Cady**[2] **and Daniel O Adams**[1]

[1] Department of Mechanical Engineering, University of Utah, 50 S Central Campus Drive Rm. 2202, Salt Lake City, UT 84112, USA
[2] Structure Property Relations Group, Los Alamos National Laboratory, Los Alamos, NM 87545, USA

E-mail: banerjee@eng.utah.edu, cady@lanl.gov and adams@eng.utah.edu

Received 5 January 2003, in final form 17 April 2003
Published 30 May 2003
Online at stacks.iop.org/MSMSE/11/457

Abstract

Polymer bonded explosives (PBXs) are particulate composites containing explosive particles and a continuous binder. The elastic modulus of the particles, at room temperature and higher, is often three to four orders of magnitude higher than that of the binder. Additionally, the explosive particles occupy high volume fractions, often greater than 90%. Both experimental and numerical determination of macroscopic properties of these composites is difficult. High modulus contrast mock PBXs provide a means of relatively inexpensive experimentation and validation of numerical approaches to determine properties of these materials. The goal of this investigation is to determine whether the effective elastic properties of monodisperse glass–estane mock PBXs can be predicted from two-dimensional micromechanics simulations using the finite element (FEM) method. In this study, the effect of representative volume element (RVE) size on the prediction of two-dimensional properties is explored. Two-dimensional estimates of elastic properties are compared with predictions from three-dimensional computations and with experimental data on glass–estane composites containing three different volume fractions of spherical glass beads. The effect of particle debonding on the effective elastic properties is also investigated using contact analyses. Results show that two-dimensional unit cells containing 10–20 circular particles are adequate for modelling glass–estane composites containing less than 60% glass particles by volume. No significant difference is observed between properties predicted by the two- and three-dimensional models. FEM simulations of RVEs, containing particles that are perfectly bonded to the binder, produce estimates of Young's modulus that are higher than the experimental data. Incorporation of debonding between particles and the binder causes the effective Young's modulus to decrease. However, the results suggest that cracks in the composite may play a

[3] Author to whom correspondence should be addressed.

significant role in determining the effective properties of mock polymer bonder explosives composed of glass and estane. The FEM simulations indicate that two-dimensional models that incorporate debonds and cracks can be used to obtain accurate estimates of the effective properties of glass–estane composites and possibly of PBXs.

1. Introduction

Polymer bonded explosives (PBXs) are extensively used as propellants in solid rocket motors. These materials are typically viscoelastic particulate composites containing high volume fractions of explosive particles suspended in a soft binder. For example, PBX 9501 contains about 92% by volume of particles. The modulus contrast between particles and the binder in PBX 9501 is around 20 000 at room temperature and low-strain-rates. The high modulus contrast between the particles and the binder as well as the high volume fraction of the particles pose an interesting challenge in the prediction of effective mechanical properties of PBXs using numerical micromechanics techniques.

The explosive nature of PBXs makes the experimental determination of their mechanical properties hazardous and thus expensive. Mock PBXs containing monodisperse glass beads and an estane binder provide an alternative material that can be tested extensively and used to provide a basis for validating micromechanics-based predictions of mechanical properties. Since the effects of high particle volume fraction and different particle sizes and shapes do not need to be considered for these glass–estane mock explosives, the evaluation of various micromechanics methods is simpler. The validated micromechanics techniques can then be applied to predict the mechanical properties of actual PBXs.

The goal of this investigation is to determine if the initial moduli of glass–estane mock PBX composites can be calculated with reasonable accuracy from the initial moduli of the constituents using finite element (FEM) analyses. The estimation of effective elastic moduli of a composite using FEMs requires the choice of a unit cell or representative volume element (RVE) that reflects the composition of the composite. The RVE is then subjected to appropriate boundary conditions and the resulting stress–strain field is averaged over the volume of the unit cell. Effective moduli are calculated from the average stress and strain fields using a linear elastic constitutive law.

This paper is organized in the following manner. The procedure used to obtain the moduli of extruded estane and glass–estane composites is discussed and the experimental data are tabulated. Next, two-dimensional unit cells containing randomly distributed particles are modelled using FEMs and the effect of RVE size on the effective properties is investigated. Three-dimensional FEM analyses are then performed on selected microstructures to determine if there exists a significant difference between two- and three-dimensional estimates. The unit cell based estimates are then compared with third-order bounds, differential effective medium estimates, and experimental data. Finally, two-dimensional simulations of the effect of particle debonding on effective elastic moduli are carried out on a selected microstructure, under both tensile and compressive loading.

2. Experimental materials

The glass–estane mock PBXs explored in this investigation are composed of spherical soda lime glass beads contained in an Estane 5703 binder.

2.1. Estane 5703

The Estane 5703 (segmented poly(ester urethane)) was obtained in pellet form from The BF Goodrich Co. Estane 5703 contains approximately 25% hard segments which are composed of 4,4-methylenediphenyl 1,1-diisocyanate (MDI) and a 1,4 butanediol chain extender. The soft segments are comprised of poly(butylene adipate). Estane has a glass transition temperature (T_g) of -31°C, a melting temperature of approximately 105°C [1]. The room temperature density of Estane 5703 is approximately $2\,\mathrm{gm\,cc^{-1}}$. Estane is known for its resistance to hydrocarbon and solvent attack, low temperature flexibility, high temperature resistance, and good adhesive properties.

2.2. Glass beads

The glass beads were manufactured by Potters (PQ Corp) Industries Inc. as a standard soda lime glass with an average diameter was $650\,\mu\mathrm{m} \pm 50\,\mu\mathrm{m}$ [2]. These glass beads are linear elastic in the range of conditions used in the experiments and have a density of $2.5\,\mathrm{gm\,cc^{-1}}$, a Young's modulus of 50 000 MPa, and a Poisson's ratio of 0.20.

2.3. Glass–estane composites

The glass–estane composites were blended on a Brabender mixer. The mixer was heated to 90°C and 100 g estane was added. The estane was heated until an elastic dough consistency was obtained. Higher temperatures caused the estane to simply coat the mixing blades. Then the glass beads were added and the sample was allowed to mix for 5–10 min. Glass beads were added to the mixture to achieve 25 wt%, 50 wt%, and approximately 65 wt% glass beads. The composite was then densified by compression moulding in a Carver hydraulic press. The sample was placed between PET sheets and heated at 90–110°C for 5 min and then the pressure was increased to 600 psi for 5 min. The 6.35 mm thick billets were then removed from the hydraulic press and rapidly cooled to room temperature.

3. Experimental procedure

Cylindrical compression specimens 6.35 mm in diameter and either 6.35 or 3.15 mm in length (L/D of 1 or 0.5) were machined for low and high-strain-rate testing, respectively, from the starting billets of the estane and the glass–estane composites. Due to the soft, viscoelastic nature of estane at ambient temperatures, a liquid nitrogen cooling procedure was employed to machine specimens with parallel loading surfaces.

3.1. Low-strain-rate compression testing

Quasi-static and low-strain-rate compression tests were conducted at strain rates of $0.001\,\mathrm{s^{-1}}$, $0.1\,\mathrm{s^{-1}}$ and $1\,\mathrm{s^{-1}}$ at temperatures from -55°C to 25°C. The compression tests were conducted with a MTS model 880 test frame with a liquid nitrogen cooled cold stage. The cold stage was operated by controlling the volume of gas passing through the loading platens. Tests were run in displacement control and the specimen strain was calculated using a displacement extensometer. Specimens were loaded to strains of approximately 30% and then unloaded. Samples were lubricated using either a thin layer of molybdenum disulfide grease, molybdenum disulfide spray lubricant, or boron nitride spray lubricant for cold temperature applications and tested in laboratory air with a relative humidity of approximately $15 \pm 4\%$.

3.2. High-strain-rate compression testing

Dynamic tests were conducted as a function of strain rate, approximately $3500\,s^{-1}$, and temperature, $-55^{\circ}C$ to $+25^{\circ}C$, utilizing a modified split-Hopkinson pressure bar (SHPB) [3, 4]. The SHPB used for this study was equipped with either 9.4-mm diameter Ti-6Al-4V or Magnesium AZ31B-alloy bars that improve the signal-to-noise level needed to test extremely low strength materials. The lower sound speed titanium and magnesium bars also help achieve sample stress equilibrium sooner, but because of the inherent oscillations in the dynamic stress–strain curves and the lack of stress equilibrium during initial load-up, the determination of yield strength must be considered inaccurate, at best, at high-strain-rates. Controlled temperature variations between $-55^{\circ}C$ and $+25^{\circ}C$ were achieved using a specially-designed gas manifold system developed at the Los Alamos National Laboratory (LANL) where samples were cooled and heated using helium (He) gas within a 304-stainless steel containment chamber held at a partial vacuum. Specimens were ramped to the desired temperature in approximately 5 min and equilibrated for approximately 10 min prior to testing. SHPB samples were lubricated with either a thin spray coating of boron nitride or a thin layer of molybdenum disulfide grease.

Due to the documented dispersive nature of wave propagation in ductile polymers and plastic-bonded composites and the potential influence of sample size on attaining a uniform stress state, the high-rate constitutive response of estane was carefully probed to obtain well-posed and accurate data. A valid, uniaxial Hopkinson bar test requires that the stress state throughout the sample achieve equilibrium during the test and this condition can be checked readily by comparing the 1-wave and 2-wave (or 3-wave) stress–strain response. When the stress state is uniform throughout the sample, then the 2-wave stress oscillates about the 1-wave stress. Additionally, relatively constant strain rates are also required for a valid SHPB test. For the current study on estane and glass–estane composites only tests meeting these criterion were deemed acceptable [5].

4. Experimental results

Representative plots of true stress versus true strain for estane and glass–estane composites are shown in figures 1(*a*) and (*b*). The elastic properties of Estane 5703 and the glass–estane mocks used in this investigation have been extracted from stress–strain data similar to those shown in figures 1(*a*) and (*b*). All FEM calculations described in this work have used prescribed strains of 0.01 in order to keep the assumption of linear elasticity valid.

The moduli of Estane 5703 shown in table 1 are for strain rates of $0.001\,s^{-1}$ and approximately $2400\,s^{-1}$ and temperatures ranging from $-55^{\circ}C$ to $23^{\circ}C$. A Poisson's ratio of 0.49 has been assumed for Estane 5703 under all conditions. The maximum modulus contrast between the glass beads and Estane 5703 is around 10 000. Initial tangent moduli from compression tests on three glass–estane composites containing 21%, 44% and 59% by volume of glass (25%, 50% and 65% by weight) are shown in table 2.

Figures 2(*a*) and (*b*) show micrographs of 44% glass–estane composites after low-strain-rate and high-strain-rate tests. It can be observed that at low-strain-rates (figure 2(*a*)) there appears to be good bonding between the glass and the estane binder though there are a few debonded particles. However, at high-strain-rates (figure 2(*b*)) the binder shows signs of shear damage and there is some damage in the glass. In this investigation, only the effect of particle–binder debonding is simulated. Fracture of the binder or of the glass beads is not considered.

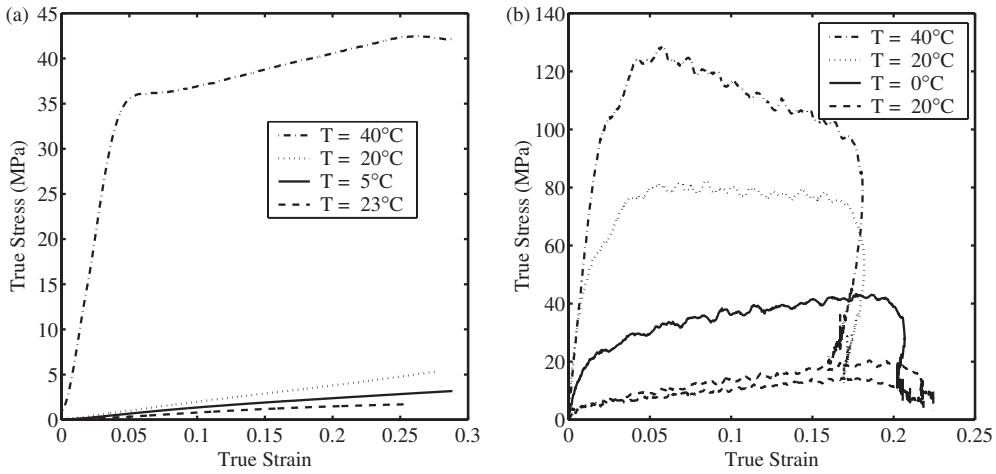

Figure 1. True stress versus true strain for glass–estane composites containing 44% glass by volume. (*a*) Low-strain-rate $\sim 0.001\,\mathrm{s}^{-1}$. (*b*) High-strain-rate $\sim 3500\,\mathrm{s}^{-1}$.

Table 1. Young's modulus of extruded Estane 5703.

	Strain rate $= 0.001\,\mathrm{s}^{-1}$					Strain rate $\sim 2400\,\mathrm{s}^{-1}$				
Temp. (°C)	−40	−30	−20	−5	23	−55	−40	−20	0	22
Modulus (MPa)	727	267	9.3	7.5	5	6250	4000	2816	2469	2439

Table 2. Young's modulus of composites containing glass and estane.

	Strain rate $= 0.001\,\mathrm{s}^{-1}$					Strain rate $\sim 3500\,\mathrm{s}^{-1}$			
				21% Glass					
Temperature (°C)	−40	−30	−20	20		−40	−20	0	20
Modulus (MPa)	526	600	10	7.5		12 000	2353	1412	857
				44% Glass					
Temperature (°C)	−40	−20	−5	23		−40	−20	0	20
Modulus (MPa)	833	18.3	11.7	6.7		5600	5600	2693	1539
				59% Glass					
Temperature (°C)	−40	−30	−20	3	23	−40	−20	0	20
Modulus (MPa)	833	394	58	28	15	6667	3415	2333	903

5. Estimation of elastic moduli

The estimation of effective elastic moduli of a composite using FEM requires the choice of a unit cell or RVE that reflects the composition of the composite. The RVE is then subjected to appropriate boundary conditions and the resulting stress–strain field is averaged over the volume of the unit cell.

The average stress and strain fields are assumed to obey the relation

$$\int_V \sigma_{ij} = C^{\mathrm{eff}}_{ijkl} \int_V \epsilon_{kl}, \tag{1}$$

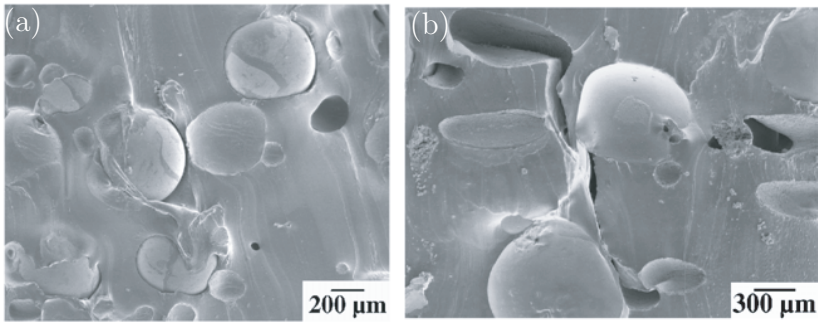

Figure 2. Debonds and cracks in glass–estane composites containing 44% glass by volume after loading. (*a*) Low-strain-rate $\sim 0.001\,\mathrm{s}^{-1}$. (*b*) High-strain-rate $\sim 3500\,\mathrm{s}^{-1}$.

where V is the volume of the unit cell, σ_{ij} are the stresses, ϵ_{ij} are the strains, and C^{eff}_{ijkl} is the effective stiffness tensor of the composite. The effective stiffness tensor can then be calculated using equation (1).

An alternative approach for determining the effective orthotropic elastic properties of the unit cell is to compute the boundary forces and displacements produced due to an applied displacement. The two-dimensional Young's moduli and Poisson's ratios can then be computed directly using relations such as

$$E_x = \frac{F_x}{u_x}, \qquad \nu_{yx} = -\frac{u_y}{u_x}, \tag{2}$$

where E_x is the modulus in the x-direction, ν_{yx} is the Poisson's ratio, F_x is the reaction force in the x-direction, u_x is the displacement in the x-direction, and u_y is the displacement in the y-direction. Equations (1) and (2) have been found to lead to the same two-dimensional effective elastic properties. A discussion of two- and three-dimensional elastic moduli is given in the monograph by Torquato [6] (p 661).

Equations (1) and (2) give two-dimensional elastic moduli for plane strain models. The upper limit on the two-dimensional Poisson's ratio is 1.0 [7]. These two-dimensional elastic moduli cannot be directly compared with experimentally obtained three-dimensional elastic moduli. Two-dimensional moduli have to be transformed into their three-dimensional form before such comparisons are made.

In this study, the two-dimensional effective Young's modulus and Poisson's ratio in the two orthogonal directions are calculated and then averaged to eliminate directional effects. The assumption is made that a plane-strain analysis of an isotropic material would lead to these average values. The three-dimensional Young's modulus and Poisson's ratio are then calculated using the relations [7]

$$\nu_{\mathrm{eff}} = \frac{\nu^{\mathrm{2D}}_{\mathrm{eff}}}{1 + \nu^{\mathrm{2D}}_{\mathrm{eff}}}, \tag{3}$$

$$E_{\mathrm{eff}} = E^{\mathrm{2D}}_{\mathrm{eff}}[1 - (\nu_{\mathrm{eff}})^2], \tag{4}$$

where ν_{eff} is the three-dimensional Poisson's ratio, E_{eff} is the three-dimensional Young's modulus, $\nu^{\mathrm{2D}}_{\mathrm{eff}}$ is the two-dimensional Poisson's ratio, and $E^{\mathrm{2D}}_{\mathrm{eff}}$ is the two-dimensional Young's modulus. This approach has been found to give estimates of Young's modulus and Poisson's ratio that are close to differential effective medium [8] estimates for volume fractions from 0.10 to 0.80 and for modulus contrasts from 10 to 100 000 [9]. It should be noted that the approach is exact for the limiting cases when the material mismatch vanishes or either of

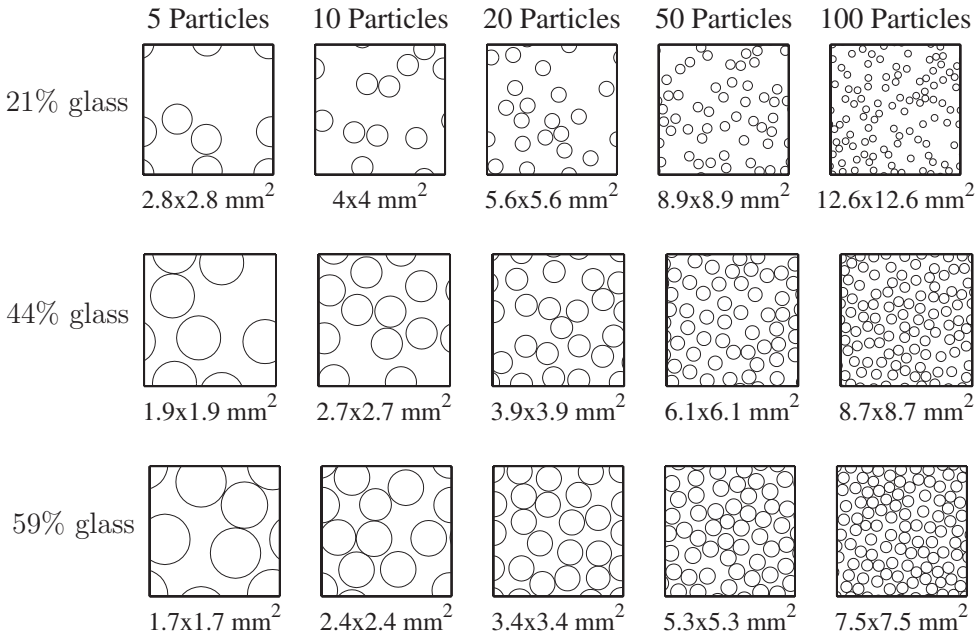

Figure 3. Sample particle distributions and unit cells of various sizes containing 21%, 44%, and 59% by volume of monodisperse circular particles. Note that the size of the unit cell increases as the number of particles increases.

the materials occupies a volume fraction of 1.0. In addition, the approach is designed only to estimate the linear elastic properties of random particulate composites.

6. Two-dimensional unit cells

The two-dimensional unit cell chosen for this study was a square box. Circular particles were placed sequentially into randomly selected positions in the unit cell. A small gap was enforced between adjacent particles so that particle–particle contact would not occur. Particles intersecting the boundary of the unit cell were repeated on opposite boundaries for periodicity of the unit cell.

The three glass–estane composites (21%, 44%, and 59% by volume of glass) were each modelled using five unit cells of increasing size that contain 5, 10, 20, 50, and 100 particles. Five different particle distributions were generated for each combination of volume fraction and number of particles in the unit cell (25 distributions for each of the three composites). Five representative particle distributions for each of the three glass–estane composites are shown in figure 3.

In this study, the FEM analysis package ANSYS [10] was used to simulate the various microstructures. A plane strain assumption was used for the two-dimensional analyses. Fixed boundary displacements (corresponding to a unidirectional strain of 1% in the RVE) and periodic displacement boundary conditions were applied along the boundaries as shown in figure 4. Periodicity requires the coupling of displacement degrees of freedom of nodes on parallel boundaries of the RVE. Coupling between nodes i and j was achieved through specified constraint equations of the form $u_i - u_j = \delta$ where u_i, u_j are displacements at nodes i and j and δ is the magnitude of the displacement constraint.

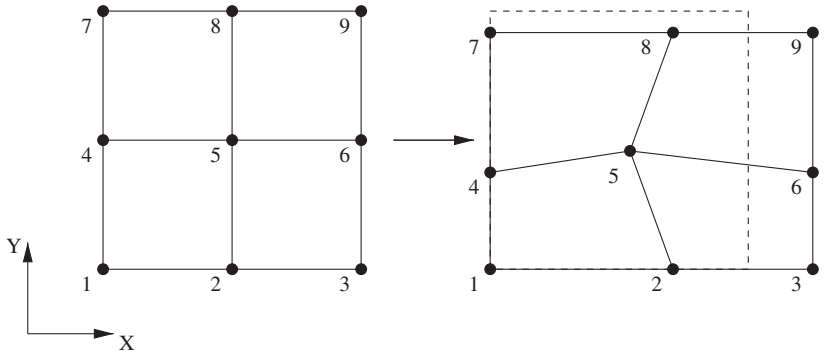

Figure 4. Displacement boundary conditions used to calculate the stress–strain behaviour of a unit cell. A uniform displacement is applied in the x-direction to nodes 3, 6, and 9. The orthogonal y-direction displacement at nodes 7, 8, and 9 are coupled so that these nodes move together.

The glass beads (particles) and the estane binder were modelled as isotropic, linear elastic materials. Six-noded, displacement-based, plane strain triangles were used to discretize the geometry of the two-dimensional unit cells. Bathe [11] has suggested the use of nine-noded mixed displacement-pressure (9–3 u/p) elements to model nearly incompressible materials such as estane. An investigation into the effect of using 9–3 u/p elements to model the rubbery binder has found that the use of such elements does not significantly affect the effective elastic moduli (compared to moduli obtained using six-noded displacement-based triangles).

6.1. Effect of unit cell size

To determine the effect of unit cell size on the effective elastic properties, two-dimensional FEM simulations were performed on particle distributions representing glass–estane mock PBXs (as shown in figure 3). The arithmetic mean of the effective Young's modulus and Poisson's ratio were calculated for five model particle distributions at each combination of volume fraction and unit cell size. Properties of glass and estane at room temperature and at a strain rate of 0.001 s^{-1} were used in the simulations.

Figures 5(*a*) and (*b*) show the variation of effective Young's modulus and Poisson's ratio with unit cell size for the glass–estane composites with three volume fractions of glass. For the composite containing 21% glass, figure 5(*a*) shows that the predicted effective Young's modulus is almost constant, both among the five models at a particular unit cell size and between different unit cell sizes. The range of variation of the effective Poisson's ratio, shown in figure 5(*b*), is also negligible for these particle distributions.

For the glass–estane composite containing 44% glass, the Young's modulus (figure 5(*a*)) does not vary much with unit cell size. Variations between different particle distributions at the same unit cell size are also negligible. Though the average effective Poisson's ratio (figure 5(*b*)) remains relatively constant with unit cell size, there is some variation between particle distributions, especially at smaller unit cell sizes.

The effective Young's modulus for a composite containing 59% glass is also shown in figure 5(*a*). In this case, the mean effective modulus varies slightly for the smaller unit cells. The variation between unit cell sizes becomes negligible for unit cells containing 10 particles or more ($\geqslant$2.4 mm). Additionally, large variations occur between particle distributions for small unit cell sizes. The variation becomes smaller for unit cells containing 50 particles or more ($\geqslant$5 mm). Similar trends are observed for the effective Poisson's ratio shown in figure 5(*b*).

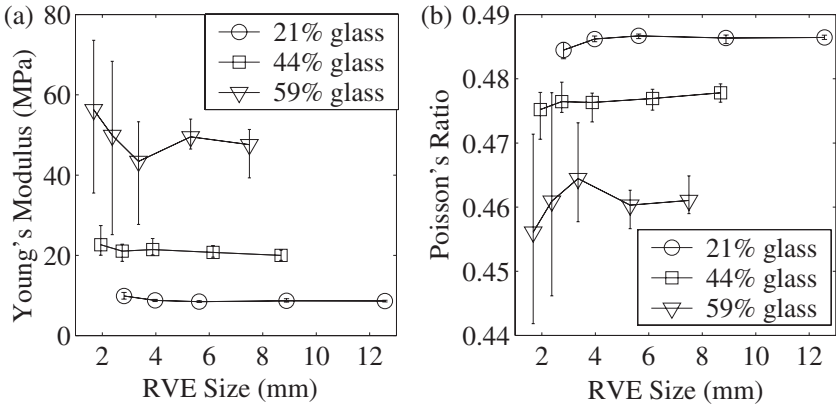

Figure 5. Variation of effective elastic properties with the size of the unit cell for a strain rate of $0.001\,s^{-1}$ and at a temperature of 23°C. (*a*) Young's Modulus. (*b*) Poisson's Ratio.

At small unit cell sizes, the variation between particle distributions is large but the mean effective Poisson's ratio stabilizes at unit cell sizes greater than 5 mm.

Results shown in figure 5 indicate that the size of the two-dimensional unit cell required to calculate the effective properties of monodisperse random composites containing circular particles is quite small. For the three volume fractions investigated, the smallest unit cell that can be used is around 4 mm in size or around six particle diameters. Results in figure 5 also show that the calculation of the effective Poisson's ratio requires a larger unit cell size than that for the effective Young's modulus. A unit cell size of around 5 mm (7.5 particle diameters) is adequate for all the volume fractions modelled. For unit cells containing 21% and 44% by volume of particles, an even smaller unit cell size can be chosen to calculate the effective Poisson's ratio. In general, a unit cell that is 6–7 particle diameters in size (or containing 10–20 particles) appears to be optimal for the calculation of effective properties of low volume fraction composites containing monodisperse circular particles. It is also observed that the appropriate RVE size increases with increase in particle volume fraction. This suggests that the RVE required to model actual PBXs (90% particles by volume) is quite large.

6.2. Convergence

Figure 6 shows the predicted effective Young's modulus of two RVEs containing 44% glass beads as a function of the number of nodes used to discretize the RVEs. The relative error in the estimate of Young's modulus is less than 2% of the value for the highest level of discretization shown in the figure when approximately 40 000 nodes are used. The number of nodes used to discretize the two-dimensional RVEs discussed in section 6 was 40 000–60 000 depending on the number of particles in the RVE.

7. Three-dimensional unit cells

Two-dimensional unit cells were used in this investigation primarily because detailed three-dimensional microstructures are difficult to generate and mesh as well as computationally expensive. The process of generating particle distributions becomes nontrivial for microstructures containing more than 45% by volume of monodisperse spheres. For higher volume

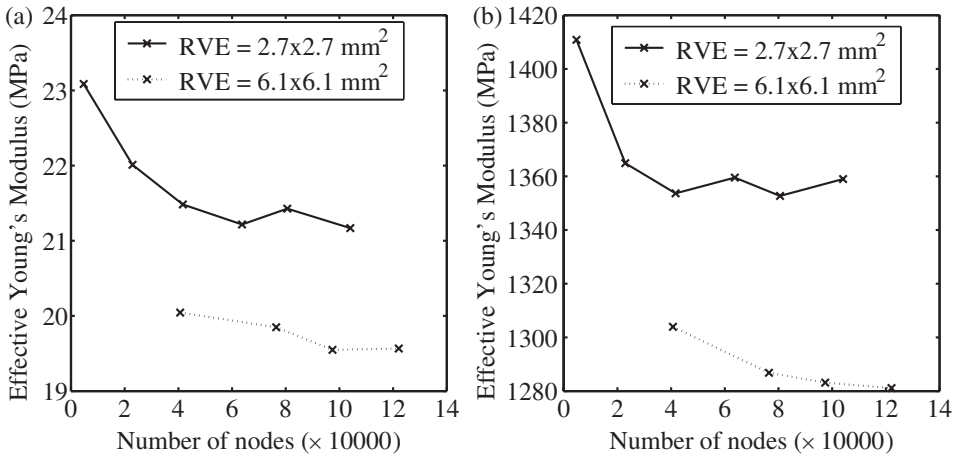

Figure 6. Variation of effective elastic properties with the number of of the nodes used to discretize the RVE. Strain rate = $0.001\,s^{-1}$. Glass volume fraction = 44%. (*a*) Temperature = 23°C. (*b*) Temperature = −40°C.

fractions even if random particle distributions can be generated, the particles are so close to each other that extremely thin elements are required to mesh the regions between particles. Since the number of elements required to discretize three-dimensional models is significantly larger than that for corresponding two-dimensional models, large computational resources are necessary for three-dimensional models. However, comparisons with three-dimensional simulations are necessary to determine if two-dimensional models adequately represent three-dimensional materials such as glass–estane composites.

To address this issue, two-dimensional FEM simulations were compared with three-dimensional FEM simulations for unit cells containing 21% and 44% spheres by volume. The three-dimensional unit cells were generated such that the length of each side was the same as that for the corresponding two-dimensional unit cell containing 10 particles. The unit cells were approximately 4 mm and 2.7 mm in size for the composites containing 21% glass and 44% glass, respectively. The 2 three-dimensional unit cells are shown in figure 7(*a*). Each of these unit cells was divided into five equal slices using dividing planes perpendicular to one direction. One such slice for each unit cell is shown in figure 7(*b*).

Due to computational limitations, FEM simulations were performed on these slices instead of the complete unit cell. Ten-noded tetrahedral elements were used to discretize the geometry of the slices. Periodic displacement boundary conditions similar to those shown in figure 4 were applied to each plane of nodes along the thickness of a slice. The boundary surfaces perpendicular to the thickness direction were constrained to remain plane and perpendicular to the thickness direction. The magnitude of the applied strain was 1%. The effective properties of the three-dimensional slices were calculated using equation (1). The results from the five slices were averaged to obtain the response of the unit cell.

To examine the effect of the number of slices on the effective properties, the three-dimensional unit cell containing 44% glass was divided into four and six slices, respectively. Estimates of effective properties were obtained for temperatures of 23°C and −40°C and a strain rate of $0.001\,s^{-1}$. These estimates show that if four slices are used, the effective Young's modulus increases by 1.7% on average (compared to using five slices). Using six slices leads

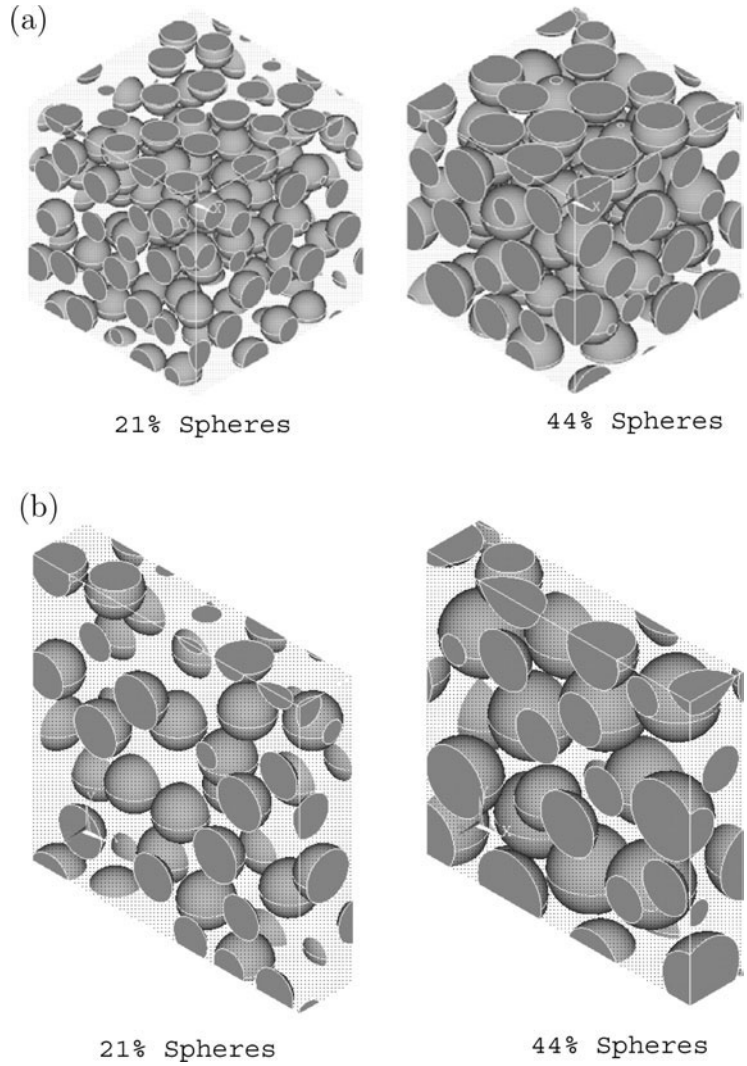

Figure 7. Three-dimensional unit cells containing 21% and 44% by volume of monodisperse circular particles and slices from the unit cells used for three-dimensional simulations. (*a*) Unit cells. (*b*) Slices of the unit cells.

to an average decrease of 1.4% in the estimate. Fewer than four slices lead to geometries that are too complex to mesh automatically and hence have not been explored.

Figure 8(*a*) shows the effective Young's modulus computed using two- and three-dimensional unit cells for 21% glass. Figure 8(*b*) shows the two- and three-dimensional unit cell based Young's modulus for 44% glass. These estimates are for a strain rate of 0.001 s^{-1}. The two- and three-dimensional predictions of Young's modulus do not differ significantly from each other. It is also observed that the three-dimensional estimates are always slightly higher than the corresponding two-dimensional estimates. The difference between the two- and three-dimensional estimates is observed to increase with increase in glass volume fraction. Similar results have been obtained for the Poisson's ratio, in which case the difference between two- and three-dimensional calculations is even smaller. Since the differences between the

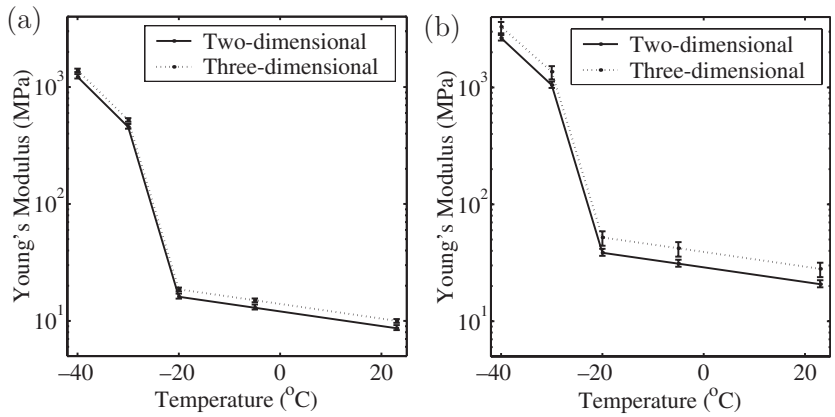

Figure 8. Young's modulus of glass–estane composites from two-dimensional and three-dimensional unit cell based FEM calculations. The estimates are for a strain rate of $0.001\,s^{-1}$. (*a*) 21% glass. (*b*) 44% glass.

two are small, the two-dimensional FEM calculations are considered sufficiently accurate for the purposes of this work.

For the same RVE size, the difference between two- and three-dimensional estimates decreases with decreasing particle volume fraction. This trend suggests that two- and three-dimensional estimates may differ considerably for high particle volume fraction PBXs. The results of some computations in this regard have been discussed elsewhere [12]. These computations show that accurate estimates of effective elastic properties of PBXs require large two-dimensional RVEs (more than $1\,cm^2$) and are extremely microstructure dependent.

7.1. Convergence

The number of nodes used to discretize the three-dimensional slices was 50 000–70 000, depending on the internal geometry of the slices. Figure 9 shows the predicted effective Young's modulus of a three-dimensional slice from a RVE containing 44% glass beads as a function of the number of nodes used. The figure shows that for the chosen level of discretization (∼60 000 nodes), the relative error in the estimate of Young's modulus is around 7% of the value for the highest level of discretization. If the convergence curve is extrapolated to 210 000 nodes, the relative error is around 10%. If the three-dimensional effective moduli shown in figure 8 are decreased by 10%, the values are closer to, but remain higher than, the two-dimensional estimates.

8. Comparison of estimates and experimental data

In this section, effective Young's moduli from two-dimensional FEM calculations are compared with third-order bounds [13] and experimental data. The FEM calculations were performed on unit cells of size approximately 9 mm, 6 mm, and 5 mm for glass–estane composites containing 21%, 44%, and 55% glass by volume, respectively (50 particles in each unit cell).

The calculation of third-order bounds requires knowledge of two geometric parameters ζ_p and η_p in addition to the volume fractions f_p and f_b of the particles and the binder.

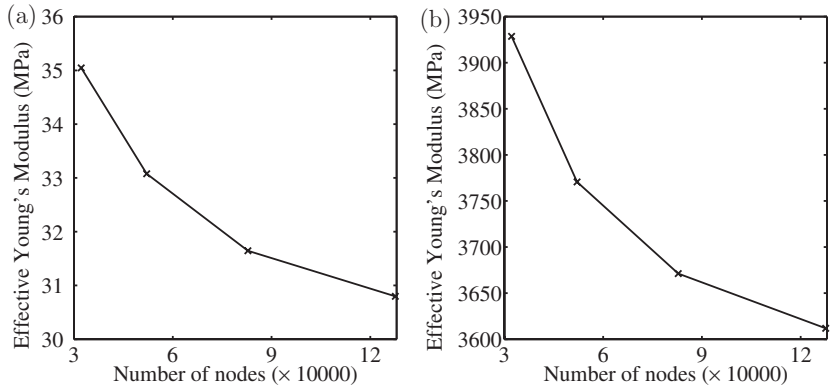

Figure 9. Variation of effective elastic properties with the number of of the nodes used to discretize a slice from a three-dimensional RVE. Strain rate $= 0.001\,\mathrm{s}^{-1}$. Glass volume fraction $= 44\%$. (*a*) Temperature $= 23^{\circ}$C. (*b*) Temperature $= -40^{\circ}$C.

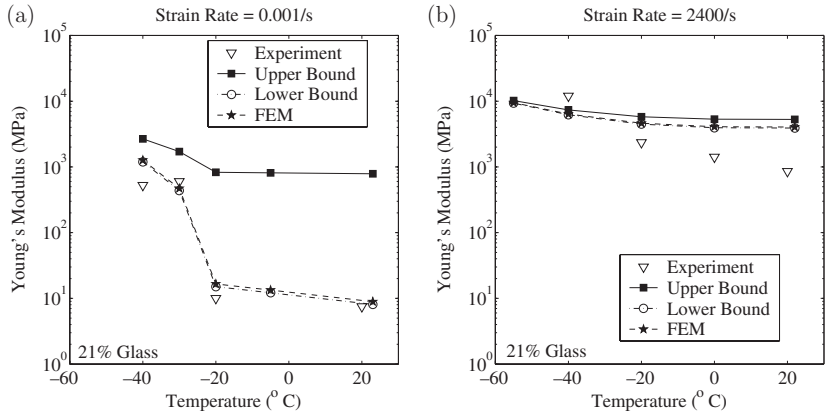

Figure 10. Comparison of experimental Young's modulus, bounds and FEM calculations for glass–estane composites containing 21% by volume of monodisperse glass beads. (*a*) Strain rate $= 0.001\,\mathrm{s}^{-1}$. (*b*) Strain rate $= 2400\,\mathrm{s}^{-1}$.

For two-component composites containing monodisperse non-overlapping spheres, these parameters are given by [6] (pp 595–619)

$$\zeta_p = \begin{cases} 0.210\,68 f_p - 0.046\,93 f_p^2 & \text{for } f_p \leqslant 0.54, \\ 0.210\,68 f_p & \text{for } 0.54 \leqslant f_p \leqslant 0.6, \end{cases} \tag{5}$$

$$\eta_p = 0.482\,74 f_p. \tag{6}$$

The third-order bounds on the Young's modulus have been calculated after determining ζ_p and η_p for the three volume fractions of glass.

Figure 10(*a*) shows the experimentally determined Young's moduli, the FEM estimates, and third-order bounds at a strain rate of $0.001\ \mathrm{s}^{-1}$ for a glass–estane composite containing 21% glass beads by volume. At low-strain-rate and ambient temperatures, there is a considerable difference between the upper and lower bounds. However, at low temperatures close to the glass transition temperature of estane, the stiffening of estane leads to a smaller modulus contrast

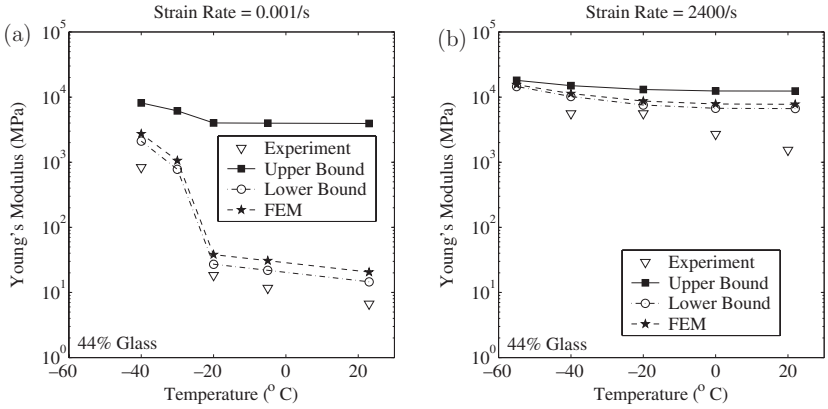

Figure 11. Comparison of experimental Young's modulus, bounds and FEM calculations for glass–estane composites containing 44% by volume of monodisperse glass beads. (*a*) Strain rate = 0.001 s^{-1}. (*b*) Strain rate = 2400 s^{-1}.

between glass and estane and the bounds are considerably closer. The FEM estimates almost coincide with the lower bounds for this volume fraction of glass. Most of the experimental Young's moduli lie below the lower bounds.

Figure 10(*b*) shows the results for a strain rate of approximately 2400 s^{-1}. The high-strain-rate experimental data for the composites are at a strain rate of approximately 3500 s^{-1} which is higher than the strain rate used to experimentally determine properties of Estane 5703 (approximately 2400 s^{-1} strain rate). It is assumed that composite properties do not vary considerably at high-strain-rates and that the experimental data for the glass–estane composites at a strain rate of approximately 3500 s^{-1} can be compared with predicted values from FEM analyses for a strain rate of approximately 2400 s^{-1}. From the high-strain-rate data shown in figure 10(*b*) it can be observed that the bounds are quite close to each other. This is because of the relatively low modulus contrast between glass and estane at these strain rates. The experimental data are again observed to be considerably lower than the lower bounds except at a temperature of -40°C in which case the experimental value of Young's modulus is two times the FEM estimate and higher than the upper bound.

Figure 11(*a*) shows the experimental data, bounds, and FEM estimates of Young's moduli for a glass–estane composite containing 44% by volume of glass at a strain rate of 0.001 s^{-1}. In this case, the FEM estimates are 1.5 to 2 times higher than the lower bounds. However, the experimental data are almost an order of magnitude lower than the FEM estimates. Figure 11(*b*) shows the experimental and predicted Young's moduli at a strain rate of 2400 s^{-1}. The bounds are quite close to each other and the FEM estimates are slightly higher than the lower bounds, but the experimental data are considerably lower than the lower bounds. The FEM estimates always lie within the third-order bounds.

Results for the glass–estane composite containing 59% by volume of glass are shown in figures 12(*a*) and (*b*). The FEM estimates are higher than the lower bound. The difference between the estimate and the lower bound is larger than for composites with lower volume fractions of glass. At a strain rate of 0.001 s^{-1}, the experimental data are quite close to the lower bound near room temperature. However, near the glass transition temperature of estane, the experimental Young's modulus is an order of magnitude lower than the FEM estimate and the lower bound. At high-strain-rates and low temperatures, the difference between FEM predictions and experimental data is less pronounced. However,

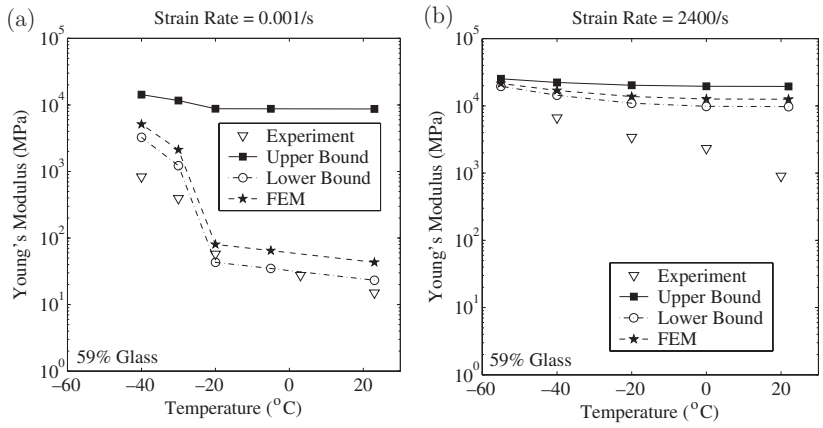

Figure 12. Comparison of experimental Young's modulus, bounds and FEM calculations for glass–estane composites containing 59% by volume of monodisperse glass beads. (*a*) Strain rate $= 0.001\,\mathrm{s}^{-1}$. (*b*) Strain rate $= 2400\,\mathrm{s}^{-1}$.

at high temperatures and high-strain-rates there is almost an order of magnitude difference between predictions and experiment.

The fact that the experimental data are lower than the lower bounds may indicate that there is considerable debonding of glass-beads from the estane binder or cracking of the binder/glass beads. The comparisons between the FEM predictions and experimental data also suggest the assumption of perfect bonding between the glass and the binder is inaccurate. Micrographs of glass–estane composites also show that there is some debonding at low-strain-rates (figure 2(*a*)). Damage in the composite appears to play a considerable role in determining effective elastic properties. This damage can be in the form of glass–binder debonds/dewetting, cracking of glass beads or cracking of the binder (figure 2(*b*)). The effect of particle debonding on the effective properties is investigated in the next section. The goal is to determine if debonding is adequate to explain the observed discrepancy between FEM estimates and experimentally determined properties of glass–estane composites.

The high-strain-rate data on Estane 5703 and the glass–estane mock explosives have been determined using stress–strain curves from SHPB impact tests. In these tests, the elastic wave moving through a test specimen reaches equilibrium some time after the specimen is impacted. Hence, the initial region of the stress–strain curve may not accurately represent the actual response of the material at small strains. This may be one of the reasons for the high estimates of modulus at high-strain-rates from FEM simulations. It is also possible that unless the loading history is taken into consideration, the effective initial moduli of viscoelastic composites at various strain rates and temperatures cannot be predicted accurately.

9. Effect of particle debonding

Two-dimensional FEM simulations were performed on the microstructure shown in figures 13(*a*) and (*b*) to investigate the effect of particle debonding on effective properties. This microstructure represents a glass–estane composite containing 44% glass by volume. Six of the particles in the microstructure are completely contained in the unit cell while the remaining four intersect the boundary.

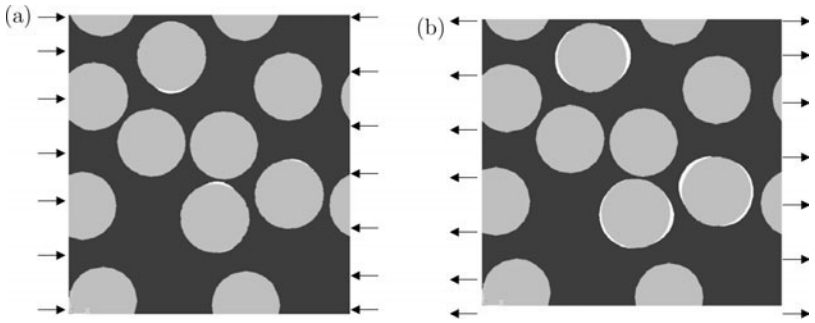

Figure 13. Debonded particles under (*a*) compression and (*b*) tension for a glass–estane composite containing 44% by volume of monodisperse glass beads with three debonded particles. Displacements shown are three times the actual. The applied strain is 1%.

The first set of simulations involved selecting one of the six completely contained particles and completely dissociating it from the surrounding material to simulate a debonded particle. The remainder of the geometry of the unit cell was meshed using six-noded triangles and the debonded particle was meshed separately. Next, two nodes on diametrically opposite sides of the debonded particle were coupled to the corresponding nodes in the adjacent mesh. The locations of these nodes were chosen so that the line joining the two nodes was perpendicular to the direction of the applied load. Contact elements were created at the hole in the unit cell and at the boundary of the debonded particle. A nonlinear contact simulation was performed on the unit cell with displacement boundary conditions similar to those shown in figure 4. A uniform inward displacement along a boundary was used to simulate compression while a uniform outward displacement was used to simulate tension. The resulting boundary forces and displacements at equilibrium were used in equations (2) to compute the effective Young's modulus and Poisson's ratio of the unit cell. The above procedure was repeated five times, with a different particle being debonded from the surrounding material in each simulation. This process was repeated with two, three, four and five debonded particles. Finally, one additional simulation was performed with all six particles debonded from the surrounding material.

The deformed shape of a unit cell with three debonded particles under a compressive load is shown in figure 13(*a*). Figure 13(*b*) shows the deformed shape of the same unit cell under a tensile load. The amount of separation of particles and binder is greater in tension than under compression. The orientation of the gap between the particles and the binder is not always aligned with the direction of applied load and can be affected considerably by the location of adjacent particles.

For each simulation, displacements simulating compression were applied first in the x-direction and then in the y-direction. The effective Young's moduli in the two directions were averaged to eliminate directional effects. The change in effective compressive Young's modulus with increasing particle debonding can be observed in figure 14(*a*). The corresponding change in the tensile Young's modulus is shown in figure 14(*b*). The data points shown in the figure represent the arithmetic mean of the effective moduli predicted for the different combinations of debonded particles at each level of debonding. The standard deviation for each data point is around 10% of the mean. The effective Young's modulus decreases with increasing particle-binder debond. However, under compression, even when 6 of the 10 particles (60% of the particles) have debonded, the effective properties predicted by FEM simulations are still higher than the experimentally determined properties. At the small strains that were applied (around 1%), it is unlikely that such a high percentage of particles debond in the actual material.

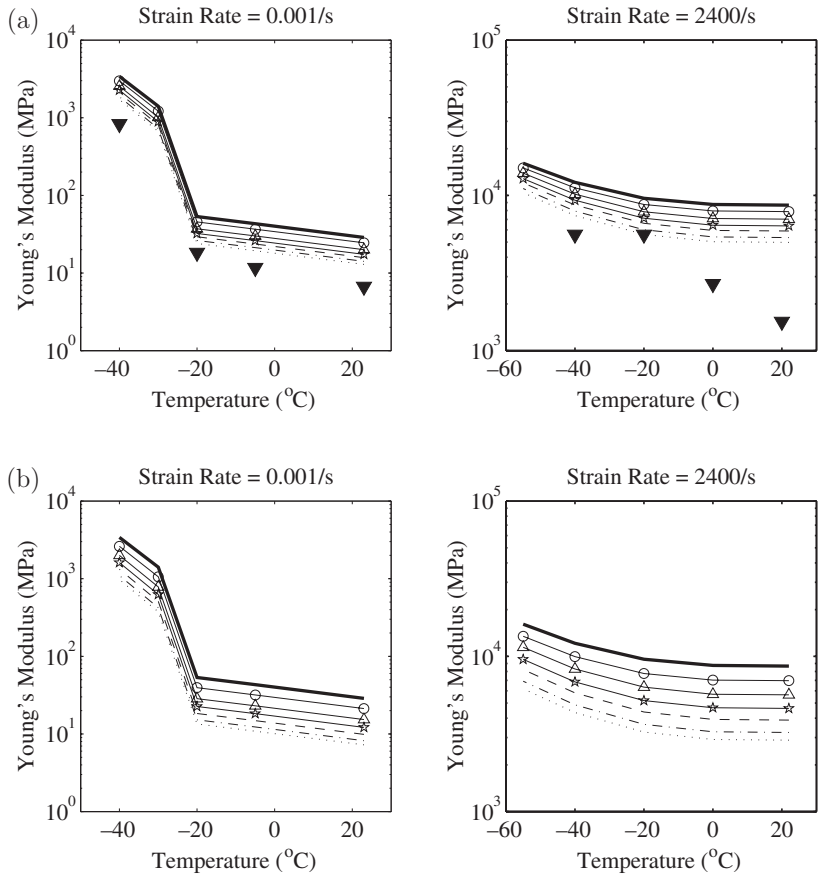

Figure 14. Effect of particle debonding on predicted values of Young's modulus of 44% glass/56% estane composite (*a*) under compression, (*b*) under tension. ▼: Expt. (compression); ——: FEM—fully bonded; ○: FEM—one particle debonded; △: FEM—two particles debonded; ★: FEM—three particles debonded; — — —: FEM—four particles debonded; — · —: FEM—five particles debonded; · · · · · ·: FEM—all six particles debonded.

The high-strain-rate results show the same qualitative effects as the low-strain-rate results. The tensile modulus decreases more rapidly with increasing debond than the compressive modulus. The compressive and tensile moduli can be considerably different for glass–estane mock PBXs in the presence of debonded particles. Experimental data from tension tests are necessary to validate the tension-based simulations.

It is possible that cracks form in the glass beads and the binder at temperatures close to the glass transition temperature of Estane, even for small applied strains at low-strain-rates. Such cracks would considerably decrease the effective stiffness of the composite in compression, presuming that the cracks were oriented randomly in all directions. One way of simulating such cracks would be to allow displacement jumps across element edges after distributing cracks randomly along element edges in the RVE. However, surface examination of the glass beads after loading at small strain rates does not indicate the presence of cracks that were not present in the unloaded material. Cracks in the binder and the glass beads are observed only at high-strain-rates, suggesting that some other physical process causes the lower stiffness of the composite.

It has also been observed that local values of strain in regions where particles are close to each other can reach as high as 20%, which is beyond the region of linear elasticity both for high-strain-rates and all temperatures and for low-strain-rates and low temperatures. These regions of high strain (possibly causing nonlinear elastic effects, plastic flow or cracking) could lead to a decrease in the effective stiffness of the composite.

10. Summary and conclusions

Experimental data on the Young's moduli of extruded Estane 5703 and glass–estane mock PBXs show strong dependence on temperature and strain rate. Two-dimensional FEM simulations based on a unit cell have been performed to determine if the initial modulus of the components of a viscoelastic, glass–estane mock PBX can be used to predict the effective initial modulus of the composite. A number of different unit cell sizes were simulated in order to determine appropriate unit cells for the glass–estane composites containing three different volume fractions of glass. It has been found that, in two dimensions, unit cells containing five to ten equal sized particles are adequate for the prediction of elastic moduli. A number of three-dimensional particle distributions have also been simulated using FEMs. The three-dimensional models predict moduli that are around 5–10% higher than the two-dimensional models. It can be concluded that two-dimensional plane strain models estimate elastic moduli of glass–estane mock explosives as accurately as three-dimensional models. The increase in RVE size with increase in particle volume fraction suggests that the RVE required for modelling PBXs (particle volume fraction greater than 0.90) is quite large and will require considerable computational resources to simulate.

Rigorous third-order bounds on the effective elastic properties of the glass–estane composites show that the experimental data are close to the lower bounds at low-strain-rates. This finding suggests that third-order lower bounds provide excellent approximations to the effective Young's modulus of low volume fraction composites with high modulus contrast at low-strain-rates. However, at high-strain-rates, except at temperatures close to the glass transition temperature of estane, the experimental moduli are considerably lower than the predicted Young's moduli. This finding suggests that there may be substantial debonding and particle/binder fracture in the composites when high-strain-rate loads are applied.

Two-dimensional FEM simulations of various glass–estane composite particle distributions also show that the predicted elastic moduli are considerably higher than the experimentally determined values. This result suggests that there may be particle-binder debonding in the glass–estane composites. Simulations performed on a model glass–estane particle distribution with increasing particle debonding have shown that increased debonding decreases the effective modulus of the composite. However, even when 60% of the particles have debonded from the surrounding material, the predicted effective moduli are higher than the experimental values. It is unlikely that such a high percentage of the particles would have debonded under the applied strain of around 1%. Therefore, particle debonding cannot fully explain the high moduli obtained from FEM simulations. It is likely that local nonlinear elastic or plastic deformation, cracks in the binder and creep or relaxation (especially at low-strain-rates) play a considerable role in determining the effective properties of glass–estane composites.

Acknowledgments

The computational aspects of this work were supported by the University of Utah Center for the Simulation of Accidental Fires and Explosions (C-SAFE), funded by the Department of Energy,

Lawrence Livermore National Laboratory, under subcontract B341493. The experimental work was performed at the Los Alamos National Laboratory by G T Gray III, W R Blumenthal and the second author. The authors would like to thank the reviewers for their helpful suggestions.

References

[1] Goodrich B F 1995 *Adhesives Technology of Estane Polyurethane* B.F. Goodrich Speciality Chemicals
[2] Potters (PQ Corp) Industries Inc. 1995 *Potters Product Lines: A Series* Potters (PQ Corp) Industries Inc. (A-055)
[3] Gray III G T, Idar D J, Blumenthal W R, Cady C M and Peterson P D 1998 High- and low-strain rate compression properties of several energetic material composites as a function of strain rate and temperature *Proc. 11th International Detonation Symp. (Snowmass, Colorado, 1998)* pp 76–84
[4] Gray III G T, Blumenthal W R, Idar D J and Cady C M 1997 Influence of temperature on the high strain rate mechanical behavior of PBX 9501 *Proc. Topical Conf. on Shock Compression of Condensed Matter* (New York: American Institute of Physics) pp 583–6
[5] Gray III G T 2000 Mechanical testing and evaluation *ASM Metals Handbook* vol 8, ed H Kuhn and D Medlin (Metals Park, Ohio: ASM International) pp 462–76
[6] Torquato S 2001 *Random Heterogeneous Materials: Microstructure and Macroscopic Properties* (New York: Springer)
[7] Jun S and Jasiuk I 1993 Elastic moduli of two-dimensional composites with sliding inclusions—a comparison of effective medium theories *Int. J. Solids Struct.* **30** 2501–23
[8] Markov K Z 2000 Elementary micromechanics of heterogeneous media *Heterogeneous Media: Micromechanics Modeling Methods and Simulations* ed K Z Markov and L Preziosi (Boston: Birkhauser) pp 1–162
[9] Banerjee B and Adams D O 2002 Micromechanics-based prediction of effective elastic properties of polymer bonded explosives *Proc. 6th Int. Conf. on Electrical Transport and Optical Phenomena in Inhomogeneous Materials (ETOPIM6) (Snowbird, Utah)*
[10] ANSYS Inc., www.ansys.com *ANSYS 6.0 User Manual*
[11] Bathe K-J 1997 *Finite Element Procedures* (Englewood Cliffs, NJ: Prentice-Hall) pp 338–88
[12] Banerjee B 2002 Micromechanics-based prediction of effective properties of high energy materials *PhD Thesis* University of Utah, Salt Lake City, Utah
[13] Milton G W 1981 Bounds on the electromagnetic, elastic and other properties of two-component composites *Phys. Rev. Lett.* **46** 542–5